Rydberg excitons in synthetic cuprous oxide Cu_2O

Stephen A. Lynch,* Chris Hodges, Soumen Mandal, and Wolfgang Langbein
School of Physics and Astronomy, Cardiff University, Cardiff CF24 3AA, United Kingdom

Ravi P. Singh
Department of Physics, Indian Institute of Science Education and Research (IISER) Bhopal, Bhopal By-pass Road, Bhauri, Bhopal 462 066, Madhya Pradesh, India

Liam A. P. Gallagher, Jon D. Pritchett, Danielle Pizzey, Joshua P. Rogers, Charles S. Adams, and Matthew P. A. Jones
Joint Quantum Centre Durham-Newcastle, Department of Physics, Durham University, Durham DH1 3LE, United Kingdom

(Received 21 October 2020; accepted 30 July 2021; published 20 August 2021)

High-lying Rydberg states of Mott-Wannier excitons are receiving considerable interest due to the possibility of adding long-range interactions to the physics of excitons. Here, we study Rydberg excitation in bulk synthetic cuprous oxide grown by the optical float zone technique and compare the result with natural samples. X-ray characterization confirms both materials are mostly single crystal, and midinfrared transmission spectroscopy revealed little difference between synthetic and natural material. The synthetic samples show principal quantum numbers up to $n = 10$, exhibit additional absorption lines, plus enhanced spatial broadening and spatial inhomogeneity. Room temperature and cryogenic photoluminescence measurements reveal a significant quantity of copper vacancies in the synthetic material. These measurements provide a route towards achieving high-n excitons in synthetic crystals, opening a route to scalable quantum devices.

DOI: 10.1103/PhysRevMaterials.5.084602

I. INTRODUCTION

The study of highly excited Rydberg exciton states facilitates an exciting crossover between two previously siloed disciplines: cold-atom physics and semiconductor quantum optics. The coherent spectroscopy of Rydberg states in gas-phase atomic systems has garnered great recent interest, with applications in the measurement of electromagnetic fields from DC to terahertz frequencies [1,2], quantum simulation [3] and computation [4], and quantum optics [5]. There is clear interest in observing similar states in semiconductor systems, where half a century of development in state-of-the-art nanofabrication techniques provide capabilities that go way beyond those available in the gas phase. Cuprous oxide raises the tantalizing prospect of a material where Rydberg atom analogues can be created on-demand in an environment that more naturally lends itself to engineering multiple quantum interactions, and furthermore offers a plausible pathway to scale up. Experiments in high-quality natural crystals have revealed the potential of cuprous oxide but realizing synthetic material with comparable quantum optical properties is a prerequisite for the material to achieve technological traction. In this paper we discuss our progress towards achieving synthetic cuprous oxide single crystals that exhibit high-n excitons.

Single-crystal cuprous oxide (Cu_2O) was one of the first semiconducting crystals used in electronics [6,7], and received considerable attention until silicon eventually prevailed as the semiconductor of choice for microelectronic applications. However, it is the unique optical properties that cause it to stand out from other semiconductor crystals. The Cu_2O band gap of 2.17 eV is about twice that of silicon, making it suited to complement silicon as a solar cell material [8]. The spectroscopic property of paramount interest to us is its extraordinary excitonic spectrum [9]. Excitons are bound electron and hole quasiparticles that exhibit a series of sharp spectral lines (not unlike the Rydberg series of hydrogen) near the semiconductor band edge. Because the exciton binding energy is typically in the meV range, the exciton lines are mostly observed at cryogenic temperatures. While it is common to observe excitons up to principal quantum numbers of $n = 3$ in conventional compound semiconductors such as GaAs [10], it has long been known that excitons with higher n can be observed in Cu_2O crystals [11]. The Cu_2O-exciton system has been used over the last three decades to test for evidence of Bose-Einstein condensation in the solid state [12], due to its forbidden exciton ground state transition.

However, it is the 2014 paper by Kazimierczuk *et al.* reporting excitons with $n = 25$ that has generated renewed interest in this material system [13]. Excitons may be described using a modified Bohr model [14,15], with the energy level spectrum described by

$$E_X(n) = -\left(\frac{\mu}{m_0}\right)\frac{1}{\epsilon_r^2}\frac{R_H}{n^2} = -\frac{R_X}{n^2}, \quad (1)$$

*LynchSA@cardiff.ac.uk

 ©2021 American Physical Society

and exciton radius,

$$\langle r_n \rangle = n^2 \left(\frac{m_0}{\mu} \right) \epsilon_r a_{\mathrm{H}} = n^2 a_{\mathrm{X}}. \tag{2}$$

Here μ is the two-body reduced mass, R_{H} and R_{X} are the hydrogen and exciton Rydberg constants, respectively, a_{H} and a_{X} are the hydrogen and exciton Bohr radii, respectively, and the other symbols have their usual meanings. For the results in [13], the relevant excitonic states give rise to the "yellow" series of transitions between the states of the uppermost valence and lowest conduction bands. Since the band states have the same parity, the excitonic energy levels have P (i.e., orbital angular momentum $l = 1$) symmetry. A narrow quadrupole transition to the dipole-forbidden $1S$ state is also observed, and phonon-assisted $1S$ transitions contribute a substantial background to the spectrum of nP states. The electron and hole effective masses are usually taken to be [16,17] $m_e = 0.99m_0$ and $m_h = 0.58m_0$, which gives $\mu = 0.37m_0$. There is some discussion over the correct value of ϵ_r to use. The high-frequency relative permittivity value is often quoted as [16] $\epsilon_r(\infty) = 6.46$, which gives $R_{\mathrm{X}} = 120.6$ meV. However, since the ground state $1S$ exciton is known to have an anomalously large binding energy [18], this value is not used. Instead, researchers use the modified Bohr formula [Eq. (1)] to fit the energies of the higher lying P excitons, yielding a smaller exciton Rydberg energy of 98.3 meV, which corresponds to $\epsilon_r = 7.2$. In reality the situation is more complicated. When the nonparabolicity of the bands, phonon coupling, and the spin interaction are properly taken into account [18], the adjusted Bohr radius of the exciton is calculated to be $a_{\mathrm{X}} = 1.11$ nm. Kazimierczuk *et al.* use this value together with an average radius $\langle r_n \rangle$ derived from the spherical harmonics of the $n = 25$ P-state wave functions to predict $\langle r_{25} \rangle = 1.04$ μm. In atomic systems, the large spatial extent of excitonic wave functions means that interactions between them are dominated by long-range van der Waals forces [19]. Unlike the short-range exchange-type interaction more commonly studied for ground state excitons, such long-range interactions can enable strong nonlocal [20] optical nonlinearities [21,22] without overlap between the excitonic wave functions. While widely studied in atomic systems [5], the first hints of such long-range interactions in crystals were observed in Kazimierczuk *et al.* [13], with subsequent confirmation via pump-probe experiments [23].

So far, however, these results [13] have not been reproduced by other groups, due to difficulties in obtaining samples of high quality. Most groups currently report on natural gemstones of various quality [Fig. 1(a)]. The highest quality synthetic samples, while reproducible, are inferior to their natural counterparts. The highest principal quantum number measured to date in a synthetic stone is $n = 10$ [24]. Wider availability of the high-quality samples required for the observation of high-n excitons is an essential step towards various quantum-optical devices based on Rydberg excitons [25–28].

Several methods for producing Cu_2O have been reported in the literature. Thin films have been prepared by several deposition methods, including reactive sputtering [29], thermal oxidation [30], electrodeposition [31,32], melting [33], and metal-organic chemical vapor deposition [34]. However, the experimental conditions necessary to observe high-n excitons impose severe constraints on the thermal expansion properties of any supporting substrate to prevent strain accumulation in the thin film on cooling to cryogenic temperatures. This is because the large spatial extent of the high-n exciton wave function should make it particularly sensitive to any distortions to the crystal lattice resulting from macroscopic strain fields [35,36]. Consequently, we have chosen to pursue a path towards macroscopic single-crystal growth using float-zone (FZ) refining, to avoid the thermal strain that would occur on cryogenic cooling if the Cu_2O was bonded to a different substrate. This method has been successfully employed in the past to produce large single crystals [24,37,38]. Our method of growth is detailed below and is similar to the method used in [38].

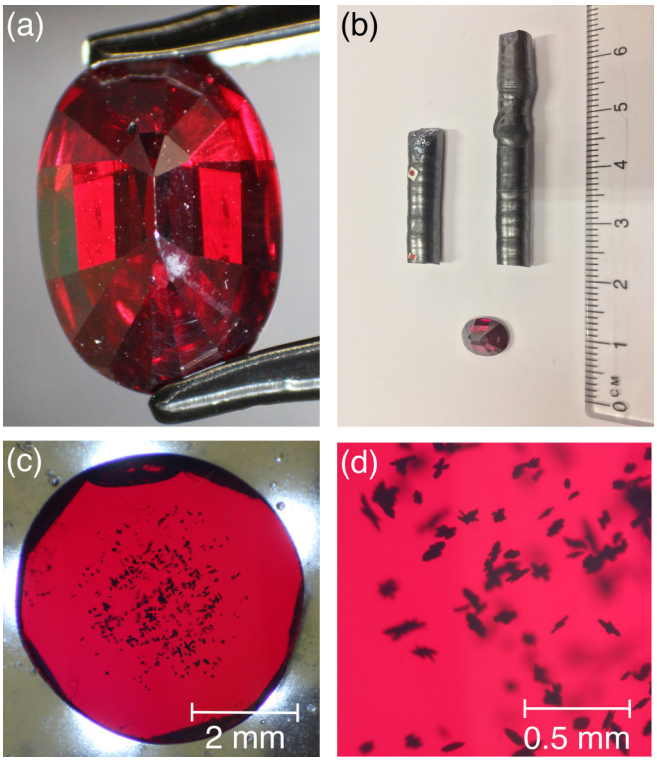

FIG. 1. (a) A commercially available natural cuprite gemstone. (b) Two synthetic single crystals of Cu_2O grown in this work with the same natural gemstone for scale. (c) Back-lit slice of optically polished synthetic crystal. (d) Higher magnification optical image of the same slice highlighting the inclusions (dark specs).

II. METHODS

A. Crystal growth

The starting material was a 5-mm-diameter copper rod, Puratronic® 99.999% (metals basis) from Alfa Aeser. The Cu_2O feed and seed rods were prepared by thermal oxidation of the copper metal rods at 1100 °C for approximately 40 h in air at atmospheric pressure. The oxidized rods were then used to grow the single-crystal material in a Crystal Systems Corporation optical furnace (model FZ-T-10000-H-VII-VPM-MII-PC). Localized heating was achieved by bringing the light from four halogen lamps to a joint focus on the sample using four semiellipsoidal mirrors. The growth

region is isolated from the furnace by a quartz tube allowing the use of different growth atmospheres and pressures; in this work we used air at atmospheric pressure. Single-crystal growth is achieved by melting a feed rod and fusing it to a seed rod, establishing a freely floating molten zone. This floating zone was then scanned up the feed rod at a controlled slow speed of 4.0–7.0 mm/h, with the feed and seed rods rotating at 20 rpm in opposite directions. This method has the advantage that it does not require a crucible, which is critical in this application because molten Cu_2O is known to react with standard crucible materials [37]. Figure 1(b) shows two 5-mm Cu_2O single crystals after FZ growth together with the same gemstone shown in (a), with a perspex laboratory ruler on the right for scale.

B. Sample preparation

For characterization, the crystals were cut into 2–3-mm-thick disks perpendicular to the cylindrical axis using a diamond saw. The samples were encapsulated in acrylic resin and lapped back to reveal the front surface of the Cu_2O. The uncovered Cu_2O surface was then polished optically flat on a Struers LaboPol-5 lapping machine, employing a four-step process using Struers consumables. Step 1 was a rough grind of the surface using a MD-Largo disk together with DiaPro Allegro/Largo 9 μm diamond suspension/lubricant for 2 min. Step 2 was a rough polish on a Struers DP-DAC satin woven acetate cloth disk together with DiaPro DAC 3 μm diamond suspension/lubricant for a further 5 min. Step 3 was a fine polishing step on a DP-NAP cloth together with a 1-μm DiaPro NAP suspension/lubricant for a further 15–30 min. Step 4 covered the final polishing, where we used a new DP-NAP cloth together with 0.25 μm DiaPro NAP suspension/lubricant. During the final polishing step, the sample was periodically inspected under a stereomicroscope, and this step was repeated until visible surface scratches/digs were removed. The other side of the sample was then lapped and polished according to the same procedure. The final thickness of the polished samples was between 50 and 100 μm for optical measurements. Thicker samples (2–3 mm), prepared in a similar way, were used for midinfrared measurements. A typical low-magnification cross-sectional image is shown in Fig. 1(c), showing homogeneous optically transparent material with the deep red signature color of Cu_2O near the outside of the disk and an increasing concentration of small dark inclusions localized towards the center. Figure 1(d) shows the same cross-sectional slice captured at greater magnification, highlighting the inclusions towards the center of the disk. These inclusions closely resemble those observed in previous works [37,39] where they were found to be voids with cupric oxide (CuO) walls.

C. X-ray analysis

X-ray analysis was performed using a Laue camera. The x-ray source was a tungsten x-ray tube. The backscattered Laue spot pattern when the (1 0 0) crystal plane is aligned perpendicular to the x-ray beam is shown in Figs. 2(b) and 2(c) for both synthetic and commercially available natural material, respectively. These Laue patterns confirm the single-crystal

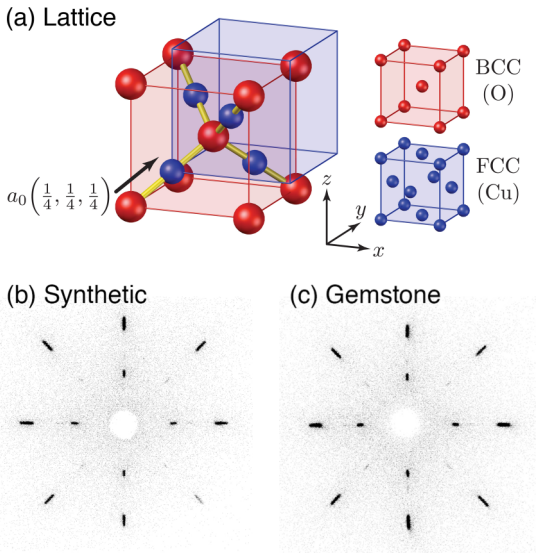

FIG. 2. (a) Interleaved bcc/fcc lattice of Cu_2O. The oxygen (O) atoms are located at the lattice points of the bcc cubic cell, while the copper (Cu) atoms lie at the lattice points of the fcc cubic cell with the same dimensions (a_0). The two cubic cells are offset by $a_0(\frac{1}{4},\frac{1}{4},\frac{1}{4})$. Laue spot pattern of both the (b) synthetic and (c) natural material for comparison. The crystals were both aligned so that the incoming beam x-ray beam is orthogonal to the (100) crystal plane. These Laue patterns highlight the cubic symmetry and single-crystal nature of both samples of Cu_2O material.

nature of both the synthetic Cu_2O material, and the natural gemstones. Cu_2O has an interleaved cubic lattice. The Cu atoms sit at the lattice points of a face-centered cubic (fcc) cell, while the oxygen atoms are located at the lattice points of a shifted body-centered cubic (bcc) lattice [40], as shown in Fig. 2(a). The expected cubic symmetry of the crystal is clear from the Laue patterns in the bottom of this figure.

D. Visible spectroscopy

The Rydberg exciton spectrum at 5 K for our synthetic material is shown in Fig. 3, along with a corresponding spectrum measured for the natural gemstone material for comparison. The samples were illuminated by a Lumileds LXML-PX02 lime-green light emitting diode with emission wavelength centered at 565 nm, limited to 570–580 nm using an Omega optical 575BP10 bandpass filter, and the exciton spectra were recorded in transmission geometry. The excitation intensity was around 10 mW/cm^2. Spectra were also recorded at lower excitation intensities to check that there were no power-dependent effects. The spectra were obtained using a custom-made imaging spectrograph with a focal length of 1.9 m. The light was dispersed by a 1200 l/mm holographic grating of (120 × 140) mm^2 size, 900 nm blaze wavelength, and detected by a CCD (Roper Pixis) of 1340 × 100 square pixels of 20 μm size. The spectrometer has a resolution of 30 μeV (FWHM) at 573 nm (2.16 eV) in second order. Sample cooling was provided by a low-vibration closed-cycle cryostat (Montana Cryostation C2) equipped with an XYZ piezo stage (Attocube) that provided a spatial resolution around 0.1 μm, allowing focusing and lateral alignment.

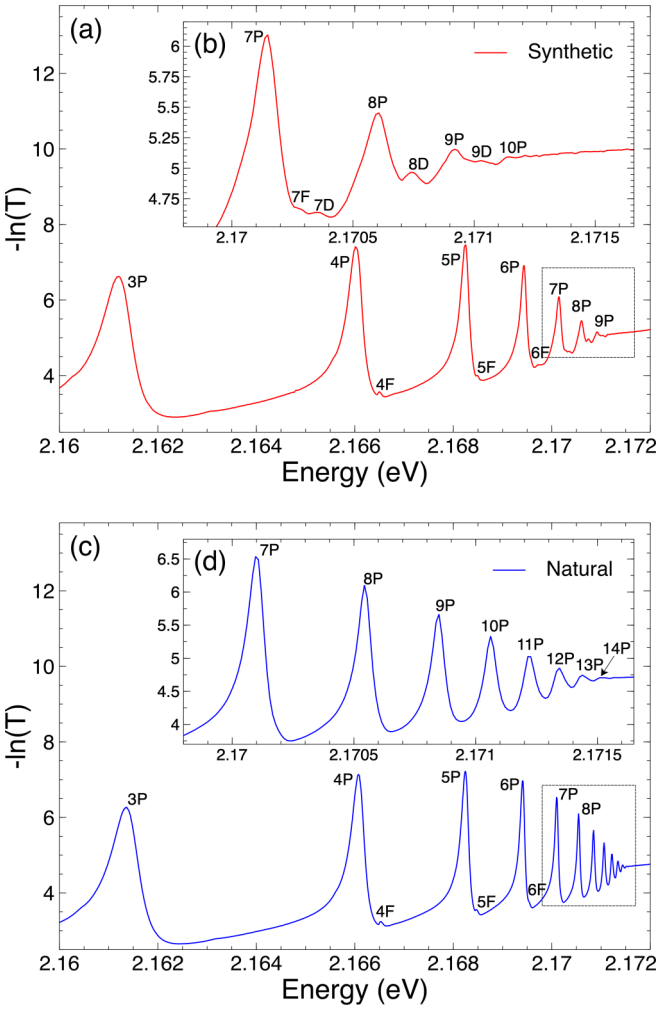

FIG. 3. Transmission spectrum for (a) synthetic (thickness 80 μm) and (c) natural (thickness 80 μm) samples of Cu_2O, measured at a nominal heat-sink temperature of 5 K. Insets (b) and (d) show the high-n regions delineated by boxes.

A Rydberg series is clearly visible in both cases, extending to $n = 9$ (possibly $n = 10$) in the synthetic material, and $n = 14$ in the natural gemstone sample. These spectra show that our synthetic material is of high quality, matching the highest principal quantum number previously observed for synthetic crystals [24]. However, exciton peaks above $n = 10$ are clearly missing. In both the natural and synthetic stones, from $n = 4$, we see small shoulders on the high-energy flank of the P states. Due to their energy, and presence only for $n \geqslant 4$, we attribute these peaks to F states [41]. However, the synthetic sample shows additional peaks between the P and F peaks. By comparing the energy of these peaks to spectra measured through two-photon spectroscopy [42] we conclude these additional peaks are D states. The observation of D states in one-photon measurements is forbidden due to parity. However, if the crystal symmetry is broken, the selection rules are broken, and forbidden angular momentum states can be observed [43,44]. Recent theoretical work has predicted that charged impurities in Cu_2O can cause the appearance of dipole-forbidden states and the disappearance of high-n states [45]. In this work the authors consider charged impurity densities up to 10^{11} cm^{-3} which was shown to limit the Rydberg series to $n = 13$. We hypothesize that our crystal has a charged impurity density exceeding 10^{11} cm^{-3} causing our spectrum to be limited to $n = 10$. In the remainder of this paper we investigate possible causes for the modified Rydberg spectrum. First we consider inhomogeneity due to strain before going on to search for point defects and vacancy impurities through photoluminescence (PL) and midinfrared absorption (MIR) spectroscopy. We find that PL spectroscopy reveals a large quantity of copper vacancies which supports our hypothesis that charged impurities are perturbing the Rydberg spectrum.

Strain leads to shifts and splittings of the exciton energy levels [46]. If the strain is spatially inhomogeneous, then averaging, for example through the thickness of the sample, can cause broadening, with the eventual loss of visibility of higher-n peaks. By fitting the peaks in Fig. 3(a) with an asymmetric Lorentzian profile [47], we find that the energies of the P states are within 30 μeV of previously reported values [13]. Figure 4 shows the exciton spectra recorded at different positions along an approximately radial cross section of the parent rod, at increments of ~100 μm. The overall structure of the exciton spectrum is remarkably uniform, with the additional peaks and the cutoff at high n showing almost no variation across the sample. Close inspection of inset 4(c) reveals slight shifts in the energy of the exciton peaks, which we analyze in more detail in Fig. 5. Here we show the difference between the local energy of the $n = 6$ peak $E_6(r)$ and its whole sample mean value $\bar{E}_6$ as a function of position for both the synthetic and natural samples. The dispersion observed for the synthetic sample is significantly larger than for our best natural sample. Here the spread in $E_6(r)$ was 18.3 μeV for the natural sample, as compared to 103.9 μeV for the synthetic sample, measured over a similar scan range. Imaging of the samples through crossed polarizers qualitatively confirms there is some macroscopic strain in the synthetic material; the samples appeared similar to those shown in [48]. This indicates that local variation in the strain does occur, but given the similarity between the spectra in Fig. 4, this does not seem a plausible explanation for the observation of dipole-forbidden exciton states and the absence of higher-n states.

E. Photoluminescence spectroscopy

Next we turn our attention to point defects, which we study using PL and MIR spectroscopy. Figure 6 shows the PL spectrum measured at room temperature. Here the excitation source was a He:Ne laser operating at 543 nm. The excitation light was tightly focused onto the sample using a microscope objective with a numerical aperture of 0.6, which also served to collect the resulting luminescence. Residual excitation light was removed using a dichroic mirror, before the PL light was coupled into multimode optical fiber and guided to a wideband grating spectrometer. The signals were carefully corrected for sample tilt and the chromatic aberration of the objective, enabling a quantitative comparison of the two samples across the full spectral range. The results are striking. For the natural sample, the dominant feature is due to quadrupole and phonon-assisted recombination of the 1S orthoexciton. For the synthetic sample, this feature is

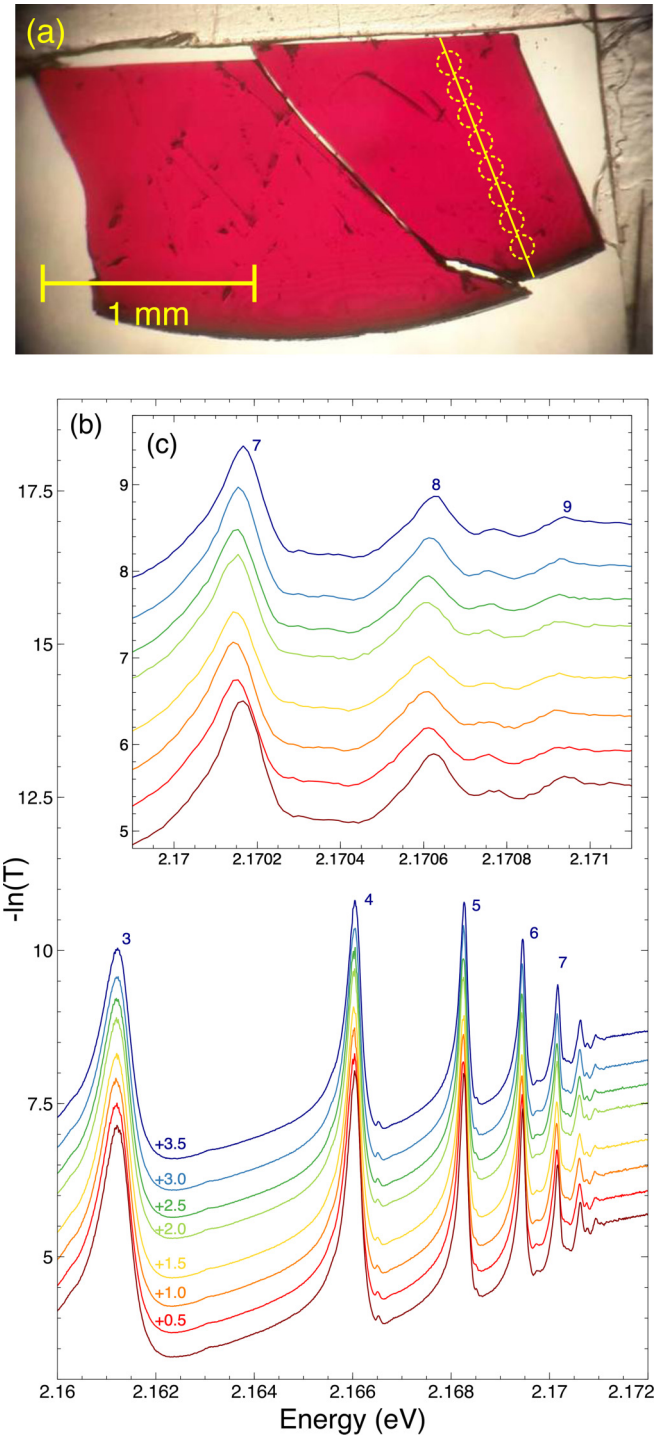

FIG. 4. (a) Low-magnification optical image of the synthetic Cu_2O sample, sandwiched between two CaF_2 coverslips and confined by a spacer of slightly greater thickness than the sample. A small drop of glue that has leaked from the spacer anchors the bottom corner of a piece of the sample on the right-hand side. The left piece of the sample is mechanically free. (b) Spectral information extracted from different positions along the approximate radial cross section of the parent rod indicated by the yellow dashed circles. Individual spectra have been offset by multiples of 0.5 to aid comparison. The inset (c) of this figure shows the same data on a magnified energy scale.

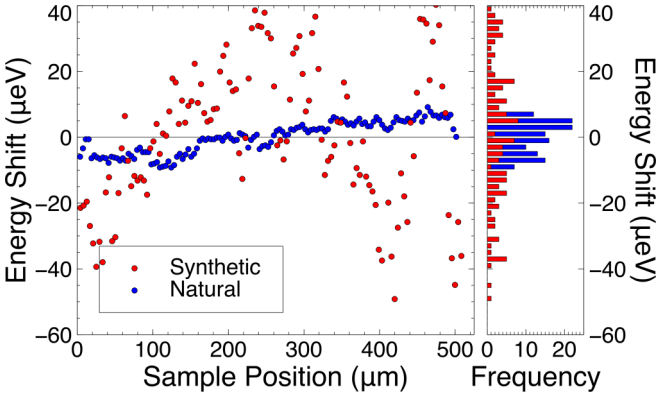

FIG. 5. Variation in the energy of the $n = 6$ peak for synthetic and natural samples, as a function of position across the sample. Here the spatial resolution was approximately 4.2 μm for the synthetic stone and 3.8 μm for the natural stone. On the right, histograms show the distribution of energy shift.

drastically reduced, and instead the spectrum is dominated by below-gap luminescence at 1.4 eV which has previously been attributed to copper vacancies [39]. Note that at 300 K, oxygen vacancies are expected to be ionized [49], and we do not see their luminescence at 1.70 eV in either sample.

To investigate these effects with higher resolution, we also performed PL measurement at low temperature using the same high-resolution spectrometer as in Fig. 3. For these measurements, the input slit aperture was 20 μm, corresponding to 1.16 μm at the sample plane. The corresponding spectral resolution is 70 μeV at 611 nm (2.01 eV) in first order. The Cu_2O was illuminated by above band gap continuous-wave low-intensity radiation ($\approx$50 μW) with wavelength $\lambda = 532$ nm. We performed a high-resolution study of the region near

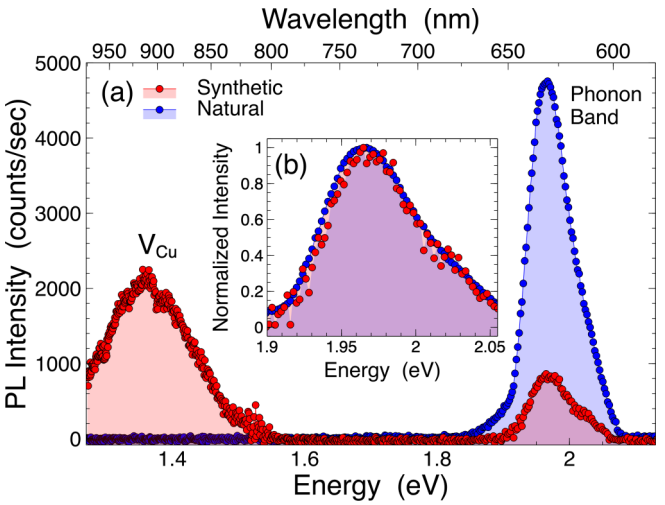

FIG. 6. (a) Broadband photoluminescence (PL) spectrum recorded at room temperature for synthetic and natural gemstone samples. A broad emission peak associated with copper vacancies (V_{Cu}) dominates the PL emission in the synthetic sample at room temperature. Inset (b): the line shape associated with the phonon emission band in both materials shows excellent agreement when normalized to the peak PL intensity as would be expected.

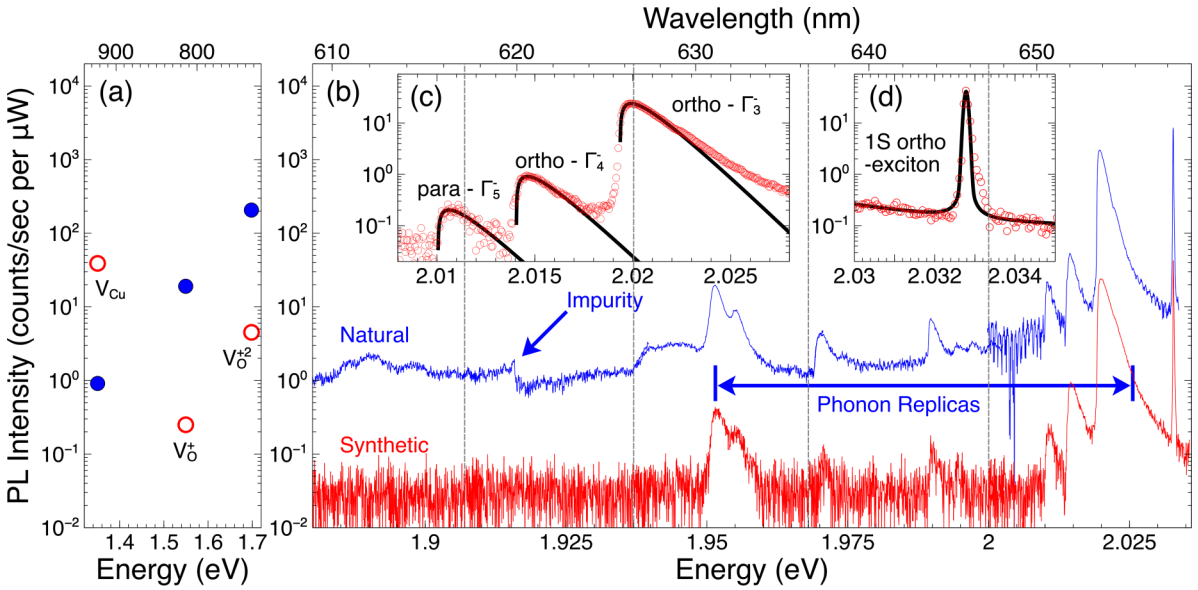

FIG. 7. High-resolution photoluminescence (PL) spectra recorded at low temperature (≈ 5 K) for synthetic (red) and natural gemstone (blue) Cu_2O normalized with respect to pump power. The subsidiary figure (a) shows the infrared PL intensity at three discrete emission wavelengths (918 n, 800, and 730 nm) associated with Cu and O vacancies, and assigned according to [50]. The main figure (b) shows the visible PL in the range 609–659 nm. The insets in this figure show (c) three phonon replicas for the synthetic material on an expanded energy scale fitted (black line) to Eq. (3), and (d) the orthophonon line fitted (black line) with a pseudo-Voigt profile also on an expanded energy scale. The lines have been assigned according to [51]. The photoluminescence was much brighter for the natural gemstone, which accounts for the signal-to-noise improvement. Two small peaks not associated with phonons were observed in the natural gemstone PL spectrum at 1.914 eV (647.8 nm) and 1.916 eV (647.1 nm), which we attribute to impurity luminescence.

the band edge [Fig. 7(b)], as well as localized measurements at energies associated with oxygen and copper vacancies [Fig. 7(a)]. The influence of excitation intensity on line shape was investigated and found to be negligible. The main effect that we observed was that the temperature of the excitons increased marginally at higher excitation intensity.

The region close to the band edge shows good agreement with previous PL studies [51,52]. The intense sharp peak at ∼2.03 eV is direct emission from the 1*S* orthoexciton line. Very similar characteristics defined this spectral line in both materials. The best fit was achieved using a pseudo-Voigt profile superimposed on the exponential Bose-Einstein tail of the first phonon replica. In both materials the line exhibited a similar asymmetry in the tails of the profile. This asymmetry is highlighted for the synthetic material in the inset of Fig. 7(d). The line fits gave a center value of 2.0328 eV for the peak and full width of 127 μeV for the synthetic material, and a center value of 2.0327 eV for the peak and full width of 135 μeV for the gemstone material. These linewidths are above our calibrated resolution limit of 70 μeV at 611 nm, and probably reflect the inhomogeneous broadening due to strain discussed earlier. The position of the 1*S* orthoexciton line is roughly 700 μeV from previously reported values [53]. As the shift is almost the same for both the natural and synthetic stones we attribute this to a systematic error in the calibration. The other large peaks in the range 1.950–2.025 eV are phonon replicas of the main 1*S* orthoexciton line [51]. The line shape of these peaks can be fitted with the convolution of two terms describing the exciton density of states (DoS) and thermal occupation statistics, respectively [54]. The low-energy side has a rising edge, which scales with the three-dimensional (3D) DoS, $g^{3D}(E)$. The high-energy side has an exponential tail from the exciton Bose-Einstein population statistics, which can be approximated to the Boltzmann distribution $f_B(E)$, since the exciton gas is of low density. The PL intensity $I_{PL} \propto g^{3D}(E) f_B(E)$ is then described by

$$I_{PL} = A(E - E_0)^{1/2} \exp\left[-\frac{(E - E_0)}{k_B T}\right], \tag{3}$$

where A is a proportionality constant and E_0 is the energy of the exciton at zero momentum minus the phonon energy, the latter assumed to be dispersionless. A similar line-shape fitting function was used in [51,52]. The fitting function gave a temperature of ∼13 K and ∼10 K for the exciton gases in the synthetic and natural samples, respectively. This is in acceptable agreement with the nominal heat-sink temperature of 5 K, because the exciton gas is expected to be at a slightly higher temperature than the crystal lattice [55]. Table I shows the energies obtained from the fitted spectral line shapes of several of the exciton phonon replicas, as well as the values reported in [51] for comparison. A theoretical phonon spectrum in Cu_2O can be found in [56] and is in good agreement with the values presented in Table I. We have not reported the energies of the Γ_5^- and $\Gamma_4^{-(1)}$(LO) phononassisted transitions in this table because we are not confident that they can be reliably deconvolved from the dominant neighboring phonon-assisted transitions in our PL data. The agreement with the values reported in [51] is otherwise excellent. We have, however, observed some differences between our natural gemstone PL spectrum and the data presented by the Kyoto group [51]. The PL spectrum in their paper shows a sharp peak located at

TABLE I. Energy positions of the phonon-assisted lines (in eV). The relative positions with respect to the resonance energy of the yellow 1*S* orthoexciton are also tabulated (in meV) and compared with the values reported in [51].

Phonon	Center (eV)	This work (meV)	[51] (meV)
Γ_5^-			10.5
Γ_3^-	2.0192	13.6	13.5
$\Gamma_4^{-(1)}$ (TO)	2.0140	18.8	18.8
$\Gamma_4^{-(1)}$ (LO)			19.3
Γ_2^-	1.9892	43.6	43.4
Γ_5^+	1.9693	63.5	63.2
$\Gamma_4^{-(2)}$ (TO)	1.9543	78.5	78.4
$\Gamma_4^{-(2)}$ (LO)	1.9507	82.1	82.0

1.947 eV, which sits on the redshifted shoulder of the double-peaked phonon feature above just 1.95 eV. We see no evidence of this spectral feature in our PL spectrum. In contrast, we observe two small sharp peaks at 1.914 and 1.916 eV, which are not present in [51]. These two peaks have been observed in previous PL studies [52,57] but have not been assigned. Unfortunately, the signal-to-noise ratio for our synthetic Cu_2O PL spectrum is insufficient to resolve these spectral features. We speculate that the origin of these peaks is due to different trace impurities to those found in the Kyoto samples. We have also recorded the intensity of the PL emission at three discrete wavelengths known to be associated with copper and oxygen vacancies [48,50] in both synthetic and natural samples [Fig. 7(a)]. Measurements at 1.35 eV (918 nm) confirm the observation of strong luminescence from copper vacancies observed in the room temperature spectrum. Measurements at 1.70 eV (800 nm) and 1.55 eV (730 nm) are associated with singly and doubly ionized oxygen vacancies, V_O^{+1} and V_O^{+2}, respectively [50]. These peaks are not observed in the room temperature data. Here we find that the luminescence from these states is strongest in the natural sample.

In summary, the region close to the band edge indicates a narrow 1*S* exciton and all the expected phonon modes in both samples. Apart from the stronger overall luminescence of the natural sample at low temperature, the spectrum of the two samples is largely identical in this region. However, the PL measurements indicate a large excess of copper vacancies in the synthetic material, which has been shown to be the result of the fabrication process (oxidation of the copper rod) [38]. We believe the copper vacancies are responsible for limiting the Rydberg series to $n = 10$ [45].

F. Mid-infrared spectroscopy

To search for other impurities that might alter the Rydberg spectrum, we also performed MIR measurements to look for shallow bound states such as those observed in silicon [58]. Much like excitons, impurity states are good sensors of the local crystal environment around the defect, and their inhomogeneous linewidth is another indicator of the material quality [59]. There is little information in the literature about the mid- and far-infrared properties of single crystal Cu_2O. A transmission spectrum for a 39.8-μm thin film was reported in [60], although many of the spectral features are obscured by Fabry-Perot interference fringes. The spectra in this work were recorded using a Bruker Vertex 80V Fourier transform spectrometer (FTS). The samples were mounted on the cold finger of a helium flow cryostat located in the spectrometer absorption compartment, and the optical path within the spectrometer was fully evacuated. Sample illumination was provided by the internal FTS globar, and the transmitted interferogram was recorded on a liquid nitrogen cooled mercury cadmium telluride (MCT) detector. Cooling was provided by a closed-cycle ColdEdge^{TM} "Stinger" helium recirculator.

Figure 8 shows the midinfrared transmission spectrum for both (a) synthetic and (c) natural samples recorded for a range of temperatures between 8 and 300 K. The samples exhibited very similar spectra with only some minor differences. The spectra are dominated by two Reststrahlen bands between 95 and 115 meV and 135 and 155 meV. Some additional peaks become more visible when the *y* axis is expanded as shown in the inset. The shoulder at 164 meV relates to the second Reststrahlen band and is present in both samples. In both cases this shoulder sharpens to a discernible peak at lower temperatures. We attribute this peak to the highest energy longitudinal optical (LO) phonon. The peak at 205 meV is also present in both samples. This peak shows a weak temperature dependence, becoming slightly sharper at lower temperature. While also present in both samples, a second peak at 215 meV appears stronger in the natural sample. The physical origin of these spectral features is open to debate. It is generally accepted that synthetically grown Cu_2O is always *p* type [61], and acceptor levels due to copper vacancies lying at 220 and 470 meV have been proposed. Previous density functional theory (DFT) calculations performed by the same research group [62] pointed towards a hole trap 450 meV above the valence band edge attributed to single copper vacancies, and a second hole trap around 250 meV tentatively attributed to a copper divacancies. We do not observe the 450-meV feature in either sample but the peaks we observe at 205 and 215 meV could fit either the copper vacancy or divacancy prediction. There is also some experimental evidence to support this hypothesis [63]. Two hole trap levels consistent with this description have been observed in the deep level transient spectrum of polycrystalline *p*-type Cu_2O epilayers grown on top of intrinsic zinc oxide (i-ZnO) and fabricated into mesa heterostructures. Theoretical calculations exploiting the generalized gradient approximation to DFT have also been used to predict a single copper vacancy level at 280 meV in *p*-type Cu_2O [64]. Another possibility is that this feature could be associated with multiphonon absorption. The spectral location matches twice the energy of the observed phonon bands, and the fact that the spectral feature is observed in two samples of completely different origin strongly suggests that it is intrinsic to the material. Multiphonon processes have previously been observed in PL spectroscopy [51,52].

III. CONCLUSIONS

In summary, there are strong similarities between the excitonic spectrum that we observe in the synthetic material and that observed in high-quality natural gemstones. The principal differences are a cutoff at lower principal quantum number,

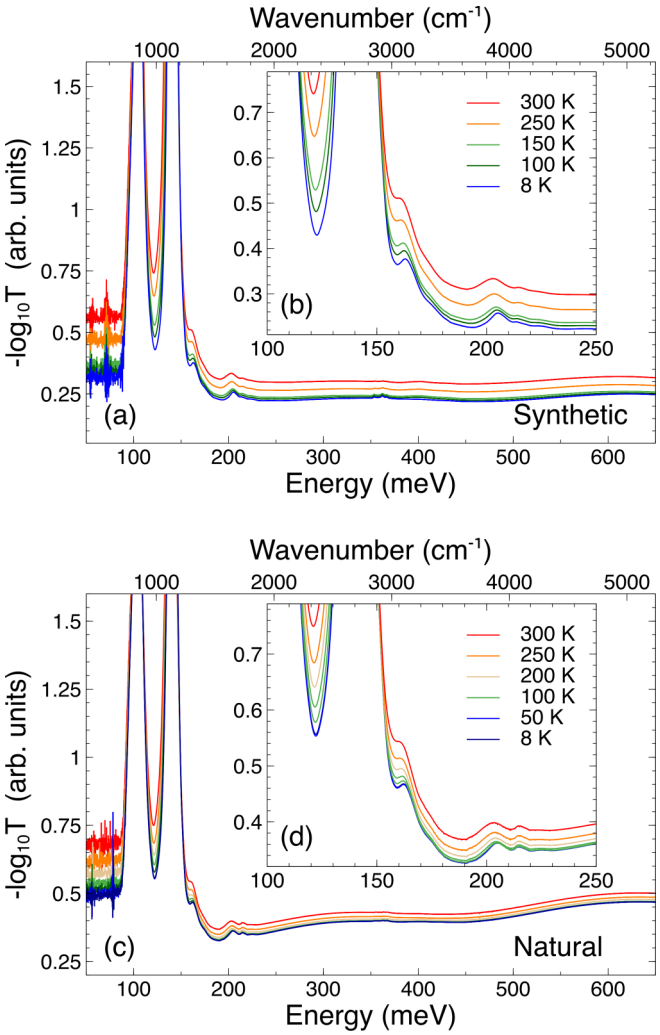

FIG. 8. (a) MIR transmission spectra of a 1-mm-thick slice of synthetic Cu_2O crystal recorded at various temperatures between 8 and 300 K. The sample was wedged at an angle of 1° to avoid Fabry-Perot fringing. The transmission T here is the ratio of the signal on the MCT detector with and without the sample, i.e., $T = I/I_0$. The increased noise below 80 meV indicates where the MCT detector response falls off at long wavelengths. The inset (b) shows the long-wavelength region near the Reststrahlen band edge on an expanded energy scale. (c) MIR transmission spectra of a similarly wedged 1-mm-thick slice of natural Cu_2O gemstone acquired at a location where high-n excitons were observed and measured under similar conditions. The inset (d) similarly shows the region near the Reststrahlen band edge on an expanded energy scale.

the emergence of dipole-forbidden peaks, and an overall shift in the spectrum. We note, however, that the observation of $n = 10$ in synthetic material is comparable to the state of the-art [24]. The large spatial extent of the high-n exciton wave functions means that they are sensitive to lattice imperfections. For example, using the formula for the Bohr radius of the P-exciton series quoted in [13], together with $a_B = 1.11$ nm, would give $\langle r_{10} \rangle = 165$ nm, which corresponds to 386 lattice constants. Measurements of the $1S$ orthoexciton width and the spatial variation of the Rydberg spectrum suggest that inhomogeneous strain cannot explain the origin of these features. We know that inhomogeneous strain fields are present in the synthetic material because we have performed some basic experiments. See the Supplemental Material [65] for a description of the experiments performed to assess the strain using crossed polarizers [66], and spatial mapping of the spectral properties associated with the $n = 6$ exciton line. PL measurements demonstrate a large excess of copper vacancies as well as the quenching of the band-edge luminescence associated with intrinsic effects in the synthetic sample. A search for additional shallow donor states in the MIR region did not produce a clear result. Our observations of an excess of copper vacancies and a modified Rydberg spectrum are in good qualitative agreement with theoretical work [45], and so we postulate that the presence of the copper vacancies is causing the changes to the Rydberg spectrum. In order for the Rydberg series to be limited to $n = 10$ the density of the copper vacancies must exceed 10^{11} cm^{-3}, which was the highest density considered in [45]. We have not attempted to address these problems yet, but there are many promising postgrowth treatments to try. For example, annealing at high temperature has been successfully employed to remove the CuO-walled voids [24,37] and reduce the concentration of copper vacancies [38,67]. The mechanical polishing procedure employed to produce samples for optical experiments may itself introduce problems that are specific to the sample origin. In the synthetic material, mechanical polishing can open some of the CuO-walled voids and this can deposit unspecified material into the polishing slurry. We have on occasion observed the appearance of new scratches and microcracking of the surface during the polishing process when this happens. However, there are fabrication strategies such as chemical etching [51] or ion-beam milling that might mitigate the consequences of this type of surface damage.

Our results are important because they demonstrate that it is possible to produce large-scale bulk synthetic material with comparable optical properties to natural gemstone material. This represents a significant step forward because it shows that there is a viable technological route towards harnessing the quantum optical properties of this extraordinary semiconductor material.

Information on the data underpinning the results presented here, including how to access them, can be found in the Cardiff University data catalog at [68].

ACKNOWLEDGMENTS

This work was supported by the Engineering and Physical Sciences Research Council (EPSRC), United Kingdom, through research Grants No. EP/P011470/1 and No. EP/P012000/1. The authors also acknowledge seedcorn funding from Durham University. L.A.P.G. acknowledges financial support from the UK Defence and Scientific Technology Laboratory via an EPSRC Industrial Case award. S.M. and R.P.S. would like to thank the Royal Society Yusuf Hamied International Exchange Award (IES/R2/181048) which has made this collaboration possible. We are grateful to Ian Chaplin and Sophie Edwards (Durham University, Department of Earth Sciences) for the slicing and polishing of some of the samples used in this work.

[1] N. Šibalić and C. S. Adams, *Rydberg Physics* (IOP Publishing, Bristol, England, 2018), pp. 2399–2891.

[2] D. H. Meyer, Z. A. Castillo, K. C. Cox, and P. D. Kunz, Assessment of Rydberg atoms for wideband electric field sensing, J. Phys. B: At., Mol. Opt. Phys. **53**, 034001 (2020).

[3] A. Browaeys and T. Lahaye, Many-body physics with individually controlled Rydberg atoms, Nat. Phys. **16**, 132 (2020).

[4] M. Saffman, Quantum computing with atomic qubits and Rydberg interactions: Progress and challenges, J. Phys. B: At., Mol. Opt. Phys. **49**, 202001 (2016).

[5] O. Firstenberg, C. S. Adams, and S. Hofferberth, Nonlinear quantum optics mediated by Rydberg interactions, J. Phys. B: At., Mol. Opt. Phys. **49**, 152003 (2016).

[6] L. O. Grondahl and P. H. Geiger, A new electronic rectifier, J. A.I.E.E. **46**, 215 (1927).

[7] L. O. Grondahl, The copper-cuprous-oxide rectifier and photoelectric cell, Rev. Mod. Phys. **5**, 141 (1933).

[8] L.-C. Chen, Review of preparation and optoelectronic characteristics of Cu_2O-based solar cells with nanostructure, Mater. Sci. Semicond. Process. **16**, 1172 (2013).

[9] E. F. Gross, Optical spectrum of excitons in the crystal lattice, Il Nuovo Cimento (1955–1965) **3**, 672 (1956).

[10] C. Weisbuch, H. Benisty, and R. Houdré, Overview of fundamentals and applications of electrons, excitons and photons in confined structures, J. Lumin. **85**, 271 (2000).

[11] P. W. Baumeister, Optical absorption of cuprous oxide, Phys. Rev. **121**, 359 (1961).

[12] D. Snoke and G. M. Kavoulakis, Bose–Einstein condensation of excitons in Cu_2O: Progress over 30 years, Rep. Prog. Phys. **77**, 116501 (2014).

[13] T. Kazimierczuk, D. Fröhlich, S. Scheel, H. Stolz, and M. Bayer, Giant Rydberg excitons in the copper oxide Cu_2O, Nature (London) **514**, 343 (2014).

[14] D. L. Dexter and R. S. Knox, *Excitons*, Interscience Tracts on Physics and Astronomy Vol. 25 (Interscience Publishers, New York, 1965).

[15] A. M. Fox, *Optical Properties of Solids*, Oxford Master Series in Condensed Matter Physics (Oxford University Press, New York, 2003).

[16] J. W. Hodby, T. E. Jenkins, C. Schwab, H. Tamura, and D. Trivich, Cyclotron resonance of electrons and of holes in cuprous oxide, Cu_2O, J. Phys. C **9**, 1429 (1976).

[17] N. Naka, I. Akimoto, M. Shirai, and K.-i. Kan'no, Time-resolved cyclotron resonance in cuprous oxide, Phys. Rev. B **85**, 035209 (2012).

[18] G. M. Kavoulakis, Y.-C. Chang, and G. Baym, Fine structure of excitons in Cu_2O, Phys. Rev. B **55**, 7593 (1997).

[19] V. Walther, S. O. Krüger, S. Scheel, and T. Pohl, Interactions between Rydberg excitons in Cu_2O, Phys. Rev. B **98**, 165201 (2018).

[20] H. Busche, P. Huillery, S. W. Ball, T. Ilieva, M. P. A. Jones, and C. S. Adams, Contactless nonlinear optics mediated by long-range Rydberg interactions, Nat. Phys. **13**, 655 (2017).

[21] M. D. Lukin, M. Fleischhauer, R. Cote, L. M. Duan, D. Jaksch, J. I. Cirac, and P. Zoller, Dipole Blockade and Quantum Information Processing in Mesoscopic Atomic Ensembles, Phys. Rev. Lett. **87**, 037901 (2001).

[22] J. D. Pritchard, D. Maxwell, A. Gauguet, K. J. Weatherill, M. P. A. Jones, and C. S. Adams, Cooperative Atom-Light Interaction in a Blockaded Rydberg Ensemble, Phys. Rev. Lett. **105**, 193603 (2010).

[23] J. Heckötter, M. Freitag, D. Fröhlich, M. Aßmann, M. Bayer, P. Grünwald, F. Schöne, D. Semkat, H. Stolz, and S. Scheel, Rydberg Excitons in the Presence of an Ultralow-Density Electron-Hole Plasma, Phys. Rev. Lett. **121**, 097401 (2018).

[24] T. Ito, H. Yamaguchi, K. Okabe, and T. Masumi, Single-crystal growth and characterization of Cu_2O and CuO, J. Mater. Sci. **33**, 3555 (1998).

[25] M. Khazali, K. Heshami, and C. Simon, Single-photon source based on Rydberg exciton blockade, J. Phys. B: At., Mol. Opt. Phys. **50**, 215301 (2017).

[26] V. Walther, R. Johne, and T. Pohl, Giant optical nonlinearities from Rydberg excitons in semiconductor microcavities, Nat. Commun. **9**, 1309 (2018).

[27] S. Zielińska-Raczyńska, G. Czajkowski, K. Karpiński, and D. Ziemkiewicz, Nonlinear optical properties and self-Kerr effect of Rydberg excitons, Phys. Rev. B **99**, 245206 (2019).

[28] V. Walther, P. Grünwald, and T. Pohl, Controlling Exciton-Phonon Interactions via Electromagnetically Induced Transparency, Phys. Rev. Lett. **125**, 173601 (2020).

[29] S. B. Ogale, P. G. Bilurkar, N. Mate, S. M. Kanetkar, N. Parikh, and B. Patnaik, Deposition of copper oxide thin films on different substrates by pulsed excimer laser ablation, J. Appl. Phys. **72**, 3765 (1992).

[30] A. O. Musa, T. Akomolafe, and M. J. Carter, Production of cuprous oxide, a solar cell material, by thermal oxidation and a study of its physical and electrical properties, Sol. Energy Mater. Sol. Cells **51**, 305 (1998).

[31] K. Santra, P. Chatterjee, and S. P. S. Gupta, Powder profile studies in electrodeposited cuprous oxide films, Sol. Energy Mater. Sol. Cells **57**, 345 (1999).

[32] A. K. Mukhopadhyay, A. K. Chakraborty, A. P. Chatterjee, and S. K. Lahiri, Galvanostatic deposition and electrical characterization of cuprous oxide thin films, Thin Solid Films **209**, 92 (1992).

[33] N. Naka, S. Hashimoto, and T. Ishihara, Thin films of single-crystal cuprous oxide grown from the melt, Jpn. J. Appl. Phys. **44**, 5096 (2005).

[34] S. Jeong and E. S. Aydil, Heteroepitaxial growth of Cu_2O thin film on ZnO by metal organic chemical vapor deposition, J. Cryst. Growth **311**, 4188 (2009).

[35] V. T. Agekyan, Spectroscopic properties of semiconductor crystals with direct forbidden energy gap, Phys. Status Solidi A **43**, 11 (1977).

[36] S. O. Krüger and S. Scheel, Waveguides for Rydberg excitons in Cu_2O from strain traps, Phys. Rev. B **97**, 205208 (2018).

[37] R. D. Schmidt-Whitley, M. Martinez-Clemente, and A. Revcolevschi, Growth and microstructural control of single crystal cuprous oxide Cu_2O, J. Cryst. Growth **23**, 113 (1974).

[38] K. B. Chang, L. Frazer, J. J. Schwartz, J. B. Ketterson, and K. R. Poeppelmeier, Removal of copper vacancies in cuprous oxide single crystals grown by the floating zone method, Cryst. Growth Des. **13**, 4914 (2013).

[39] L. Frazer, K. B. Chang, K. R. Poeppelmeier, and J. B. Ketterson, Cupric oxide inclusions in cuprous oxide crystals grown by the floating zone method, Sci. Technol. Adv. Mater. **16**, 034901 (2015).

[40] B. K. Meyer, A. Polity, D. Reppin, M. Becker, P. Hering, B. Kramm, P. J. Klar, T. Sander, C. Reindl, C. Heiliger, M.

Heinemann, C. Müller, and C. Ronning, The physics of copper oxide (Cu_2O), in *Oxide Semiconductors*, Semiconductors and Semimetals Vol. 88, edited by B. G. Svensson, S. J. Pearton, and C. Jagadish (Elsevier, New York, 2013), pp. 201–226.

[41] J. Thewes, J. Heckötter, T. Kazimierczuk, M. Aßmann, D. Fröhlich, M. Bayer, M. A. Semina, and M. M. Glazov, Observation of High Angular Momentum Excitons in Cuprous Oxide, Phys. Rev. Lett. **115**, 027402 (2015).

[42] J. Mund, D. Fröhlich, D. R. Yakovlev, and M. Bayer, High-resolution second harmonic generation spectroscopy with femtosecond laser pulses on excitons in Cu_2O, Phys. Rev. B **98**, 085203 (2018).

[43] J. Heckötter, M. Freitag, D. Fröhlich, M. Aßmann, M. Bayer, M. A. Semina, and M. M. Glazov, Scaling laws of Rydberg excitons, Phys. Rev. B **96**, 125142 (2017).

[44] J. Heckötter, M. Freitag, D. Fröhlich, M. Aßmann, M. Bayer, M. A. Semina, and M. M. Glazov, Influence of the wavefunction distribution on exciton dissociation in electric field, Phys. Solid State **60**, 1506 (2018).

[45] S. O. Krüger, H. Stolz, and S. Scheel, Interaction of charged impurities and Rydberg excitons in cuprous oxide, Phys. Rev. B **101**, 235204 (2020).

[46] H. R. Trebin, H. Z. Cummins, and J. L. Birman, Excitons in cuprous oxide under uniaxial stress, Phys. Rev. B **23**, 597 (1981).

[47] Y. Toyozawa, Theory of line-shapes of the exciton absorption bands, Prog. Theor. Phys. **20**, 53 (1958).

[48] L. Frazer, E. J. Lenferink, K. B. Chang, K. R. Poeppelmeier, N. P. Stern, and J. B. Ketterson, Evaluation of defects in cuprous oxide through exciton luminescence imaging, J. Lumin. **159**, 294 (2015).

[49] S. Koirala, N. Naka, and K. Tanaka, Correlated lifetimes of free paraexcitons and excitons trapped at oxygen vacancies in cuprous oxide, J. Lumin. **134**, 524 (2013).

[50] L. Frazer, K. B. Chang, R. D. Schaller, K. R. Poeppelmeier, and J. B. Ketterson, Vacancy relaxation in cuprous oxide ($Cu_{2-x}O_{1-y}$), J. Lumin. **183**, 281 (2017).

[51] M. Takahata and N. Naka, Photoluminescence properties of the entire excitonic series in Cu_2O, Phys. Rev. B **98**, 195205 (2018).

[52] Y. Petroff, P. Y. Yu, and Y. R. Shen, Study of photoluminescence in Cu_2O, Phys. Rev. B **12**, 2488 (1975).

[53] L. Frazer, K. B. Chang, K. R. Poeppelmeier, and J. B. Ketterson, Photoionization cross section of 1*s* orthoexcitons in cuprous oxide, Phys. Rev. B **89**, 245203 (2014).

[54] R. J. Elliott, Intensity of optical absorption by excitons, Phys. Rev. **108**, 1384 (1957).

[55] J. P. Wolfe and J. I. Jang, The search for Bose–Einstein condensation of excitons in Cu_2O: Exciton-Auger recombination versus biexciton formation, New J. Phys. **16**, 123048 (2014).

[56] P. A. Korzhavyi and B. Johansson, Literature review on the properties of cuprous oxide Cu_2O and the process of copper oxidation, Technical Report No. SKB TR-11-08 (Department of Materials Science and Engineering, Royal Institute of Technology, Stockholm, 2011).

[57] K. E. O'Hara, Relaxation kinetics of excitons in cuprous oxide, Ph.D. thesis, University of Illinois, 1999.

[58] C. Jagannath, Z. W. Grabowski, and A. K. Ramdas, Linewidths of the electronic spectra of donors in silicon, Phys. Rev. B **23**, 2082 (1981).

[59] S. A. Lynch, G. Matmon, S. G. Pavlov, K. L. Litvinenko, B. Redlich, A. F. G. van der Meer, N. V. Abrosimov, and H.-W. Hübers, Inhomogeneous broadening of phosphorus donor lines in the far-infrared spectra of single-crystalline SiGe, Phys. Rev. B **82**, 245206 (2010).

[60] M. O'Keeffe, Infrared optical properties of cuprous oxide, J. Chem. Phys. **39**, 1789 (1963).

[61] D. O. Scanlon and G. W. Watson, Undoped n-type Cu_2O: Fact or fiction?, J. Phys. Chem. Lett. **1**, 2582 (2010).

[62] D. O. Scanlon, B. J. Morgan, G. W. Watson, and A. Walsh, Acceptor Levels in *p*-Type Cu_2O: Rationalizing Theory and Experiment, Phys. Rev. Lett. **103**, 096405 (2009).

[63] G. K. Paul, Y. Nawa, H. Sato, T. Sakurai, and K. Akimoto, Defects in Cu_2O studied by deep level transient spectroscopy, Appl. Phys. Lett. **88**, 141901 (2006).

[64] H. Raebiger, S. Lany, and A. Zunger, Origins of the *p*-type nature and cation deficiency in Cu_2O and related materials, Phys. Rev. B **76**, 045209 (2007).

[65] See Supplemental Material at http://link.aps.org/supplemental/10.1103/PhysRevMaterials.5.084602 for describing additional experiments performed to assess the strain using crossed polarizers and spatial mapping of the spectral properties associated with the $n = 6$ exciton line.

[66] A. S. Redner, Nondestructive evaluation using polarized light, Mater. Eval. **53**, 642 (1995).

[67] R. G. Kaufman and R. T. Hawkins, Annealing of copper and oxygen vacancies in cuprous oxide films monitored by low temperature luminescence, J. Electrochem. Soc. **133**, 2652 (1986).

[68] http://doi.org/10.17035/d.2021.0138814630.